photonics

MDPI

Article

Unified Modeling of Irradiance Scintillation for Laser Beams in Arbitrary Oceanic Turbulence

Bingyan Fu †, Wanqi Zhang †, Taiming Hu, Guangqing Liu, Yuxuan Li and Xiang Yi *

School of Communications Engineering, Xidian University, Xi'an 710071, China; 23012100006@stu.xidian.edu.cn (B.F.); 23012100058@stu.xidian.edu.cn (W.Z.); 23012100040@stu.xidian.edu.cn (T.H.); gql@stu.xidian.edu.cn (G.L.); lyuxuan@stu.xidian.edu.cn (Y.L.)

* Correspondence: yixiang@xidian.edu.cn

† These authors contributed equally to this work.

Abstract

Accurate modeling of irradiance scintillation is important for evaluating underwater wireless optical communication (UWOC) systems operating in oceanic turbulence. Existing studies have mainly focused on weak oceanic turbulence conditions, while irradiance scintillation modeling under arbitrary oceanic turbulence strength remains insufficiently developed. In this work, the Gaussian beam is adopted as the representative model of practical laser beams, whereas the plane-wave and spherical-wave cases are introduced as limiting cases to support the derivation and theoretical completeness of the Gaussian-beam formulation. A unified theoretical framework is developed based on the general oceanic turbulence optical power spectrum (OTOPS). Building upon previously reported weak-turbulence results, the scintillation index (SI) under saturated strong turbulence is first derived using asymptotic theory. Then, within the extended Rytov approximation, an effective-scale treatment is introduced to characterize the contributions of large- and small-scale eddies to irradiance fluctuations. By connecting the weak- and saturated-turbulence limits through asymptotic matching, a closed-form SI expression valid over a wide range of oceanic turbulence strengths is obtained. Numerical results show that the proposed model agrees well with the corresponding boundary cases and reproduces the characteristic "bump" behavior of oceanic turbulence, while highlighting the influence of ocean-specific cutoff spatial frequencies on the predicted scintillation peaks. These results provide a physically consistent analytical framework for UWOC channel modeling and performance evaluation under arbitrary oceanic turbulence strength.

Keywords: irradiance scintillation; channel modeling; underwater wireless optical communication; bit error rate; oceanic turbulence optical power spectrum

Check for updates

Received: 17 April 2026
Revised: 7 May 2026
Accepted: 9 May 2026
Published: 11 May 2026

Copyright: © 2026 by the authors. Licensee MDPI, Basel, Switzerland. This article is an open access article distributed under the terms and conditions of the Creative Commons Attribution (CC BY) license.

1. Introduction

With the growing demand for marine resource exploration, environmental monitoring, and cooperation among underwater platforms, increasing attention has been paid to communication technologies that can provide high speed, low latency, and reliable transmission underwater. Compared with traditional acoustic and radio-frequency communication, underwater wireless optical communication (UWOC) offers higher bandwidth, lower latency, and better security, and is therefore considered a promising solution for short- and medium-range high-speed underwater links [1–3].

In real ocean environments, optical propagation is affected by absorption, scattering, and oceanic turbulence. Among them, oceanic turbulence causes random fluctuations

in the refractive index of seawater, which may further lead to beam spreading, beam wandering, and irradiance fluctuations at the receiver [4–6]. Irradiance fluctuations are usually quantified by the scintillation index, which directly influences the system signal-to-noise ratio (SNR), bit error rate (BER), and link stability [5]. In the present model, we mainly focus on the on-axis irradiance scintillation along the propagation direction, while beam wandering is mainly associated with transverse beam displacement and radial scintillation. It is not included in the current analysis and will be developed in the near future. For this reason, developing a physically consistent theoretical model for SI is an important basis for UWOC channel modeling and system performance analysis.

In underwater optical channels, absorption, scattering, and oceanic turbulence jointly determine the propagation characteristics. Monte Carlo-based methods have been widely used to characterize absorption-, scattering-, turbidity-, and non-homogeneous-water effects in underwater optical links [7,8]. These methods are useful for obtaining channel characteristics in complex underwater environments. In contrast, the present work focuses on irradiance scintillation induced by random refractive-index fluctuations of seawater, which is mainly a wave-optics effect.

One of the key issues in the study of optical propagation through oceanic turbulence is the power spectrum model of refractive-index fluctuations. The Nikishov spectrum provided an early foundation for oceanic turbulence studies [9], and later work further extended it by considering the eddy diffusivity ratio, the range of Prandtl/Schmidt numbers, and practical spectrum approximations [10–12]. On this basis, Yao et al. proposed the oceanic turbulence optical power spectrum (OTOPS), which is applicable to arbitrary average temperature, average salinity concentration, and wavelength, and provides a more unified theoretical basis for studying light propagation and scintillation in oceanic turbulence [10].

Based on these spectrum models, many studies have investigated the scintillation behavior of plane waves, spherical waves, and Gaussian beams in oceanic turbulence [13–15]. Among them, Gaussian beams are of greater engineering interest because they are closer to the output field of practical laser transmitters used in UWOC systems. Therefore, in this work, the Gaussian beam is adopted as the representative model of practical laser beams. The plane-wave and spherical-wave cases are introduced as limiting cases and auxiliary solutions for deriving and verifying the Gaussian-beam scintillation model. Li et al. developed a general expression for the scintillation index of Gaussian beams propagating through oceanic turbulence based on the general OTOPS model and further analyzed its impact on UWOC system performance. Their work provides an important foundation for modeling Gaussian laser beams under weak oceanic turbulence [16].

However, most existing studies still focus on the weak-turbulence regime, and a unified SI model valid for arbitrary oceanic turbulence intensity is still lacking. As the propagation distance increases or the turbulence becomes stronger, irradiance fluctuations may evolve from weak fluctuations to moderate-to-strong turbulence and even the saturation region. In addition, the boundaries between weak, moderate, strong, and saturated oceanic turbulence are often operational or experience-based, rather than being defined by a universally accepted rigorous standard. Therefore, it may be difficult to determine reliably which turbulence regime a practical propagation scenario belongs to, especially when the propagation distance and oceanic turbulence parameters vary. Under such conditions, a unified model is useful not only for describing the weak-to-saturated transition but also for reducing the dependence on ad hoc regime classification and segmented model selection.

Motivated by this, this paper develops a unified closed-form model for the scintillation index (SI) of Gaussian laser beams under arbitrary oceanic turbulence strength based on the general OTOPS. The weak-turbulence result in [13] is adopted as the low-fluctuation

boundary, and the saturated strong-turbulence boundary is further derived. By combining extended Rytov interpolation with asymptotic matching, a closed-form SI expression connecting the weak, moderate-to-strong, and saturated regimes is obtained. The main novelty of this work lies in deriving a unified Gaussian-beam SI model under the general OTOPS framework and re-determining the ocean-specific cutoff spatial frequencies, rather than directly inheriting the atmospheric cutoff-frequency treatment. The proposed model is examined in terms of asymptotic boundary consistency and comparison with existing analytical formulations, thereby providing a theoretical basis for UWOC channel modeling and performance evaluation.

2. Model Formulation

2.1. Saturated-Turbulence Boundary Model

In our previous work [16], the scintillation characteristics of Gaussian beams under weak oceanic turbulence were investigated within the Rytov framework, where a closed-form expression for the scintillation index (SI) was derived. This previous result is used here only as the low-fluctuation boundary condition, while the present work further derives the saturated-turbulence boundary and constructs a unified weak-to-saturated SI model through extended Rytov interpolation and asymptotic matching. Therefore, the present manuscript extends the previous weak-turbulence Gaussian-beam analysis. To extend the analysis to the saturated regime, asymptotic theory is employed. Based on this framework, the longitudinal scintillation index of a Gaussian beam under saturated oceanic turbulence can be expressed as [6].

$$\begin{aligned}\sigma_S^2(0,L) = 1 + 32\pi^2k^2L\int_0^1\int_0^\infty \kappa\Phi_n(\kappa)\sin^2\left[\frac{L\kappa^2}{2k}\xi\left(1-\overline{\Theta}\xi\right)\right] \\ \times\exp\left(-\frac{\Lambda L\kappa^2\xi^2}{k}\right)\exp\left\{-\int_0^1 D_S\left[\frac{L\kappa}{k}w(\tau,\xi)\right]d\tau,\right\}d\kappa d\xi\end{aligned} \tag{1}$$

where $\sigma_s^2(0,L)$ is the longitudinal scintillation index on the propagation axis after a propagation distance L; L denotes the propagation distance; $k = 2\pi/\lambda$ is the optical wavenumber, where λ is the optical wavelength; κ denotes the magnitude of the transverse spatial frequency; $\Phi_n(\kappa)$ is the oceanic refractive-index fluctuation power spectrum; and ξ and τ are dimensionless path variables along the propagation direction. In addition, Θ and Λ are dimensionless Gaussian-beam parameters related to the initial wavefront curvature and diffraction effect, respectively, and their detailed definitions can be found in [6]; $D_s(\rho)$ represents the plane-wave phase structure function, where ρ is the transverse separation. The second exponential term in Equation (1) can therefore be interpreted as a low-pass spatial filter determined by $D_s(\rho)$. The auxiliary function $w(\tau,\xi)$ is defined as

$$w(\tau,\xi) = \begin{cases}\tau\left(1-\overline{\Theta}\xi\right), \tau < \xi \\ \xi\left(1-\overline{\Theta}\tau\right), \tau > \xi\end{cases}. \tag{2}$$

The low-pass filtering effect in (1) ensures that the dominant contribution is restricted to the region $L\kappa^2/k \ll 1$, and, therefore, the geometric optics approximation can be applied. Under this condition, the phase structure function can be approximated by the corresponding wave structure function in the near-field region. Accordingly, the following approximations hold [6]

$$\sin^2\left[\frac{L\kappa^2}{2k}\xi\left(1-\overline{\Theta}\xi\right)\right] \cong \frac{L^2\kappa^4}{4k^2}\xi^2\left(1-\overline{\Theta}\xi\right)^2,\ \exp\left(-\frac{\Lambda L\kappa^2\xi^2}{k}\right) \cong 1. \tag{3}$$

The second approximation in (3) indicates that, in the saturated regime, the beam spreads sufficiently so that the longitudinal scintillation behavior approaches that of a large-diameter wave with nearly uniform amplitude. As a result, the Gaussian beam parameter Λ effectively disappears from the SI expression. By substituting (3) into (1), the longitudinal SI can be simplified as

$$\sigma_S^2(0,L) = 1 + 8\pi^2 L^3 \int_0^1 \int_0^\infty \kappa^5 \Phi_n(\kappa) \xi^2 \left(1 - \overline{\Theta}\xi\right)^2 \exp\left\{ -\int_0^1 D_S\left[\frac{L\kappa}{k} w(\tau,\xi)\right] d\tau \right\} d\kappa d\xi. \tag{4}$$

Because of the mathematical complexity of (4), it is convenient to first consider the special cases of plane waves and spherical waves. For a plane wave ($\overline{\Theta} = 0$), using Formula (4) and the general OTOPS [17], the SI of the plane wave within the saturated region can be calculated

$$\sigma_{S,pl}^2(L) = 1 + 2\pi\beta_0 \varepsilon^{-1/3} L^3 \left(A^2 \chi_T W_{T,pl} + B^2 \chi_S W_{S,pl} + 2AB\chi_{TS} W_{TS,pl} \right), \tag{5}$$

where the $W_{i,pl}$ is

$$\begin{cases} W_{i,pl} = \int_0^1 \xi^2 \left\{ \dfrac{0.4639}{\left[sim_{pl,i}(\xi)\right]^{\frac{7}{6}}} + \dfrac{0.4428\Delta_{1,i}}{\left[sim_{pl,i}(\xi)\right]^{\frac{7}{6}+\frac{0.61}{2}}} - \dfrac{0.4429\Delta_{2,i}}{\left[sim_{pl,i}(\xi)\right]^{\frac{7}{6}+\frac{0.55}{2}}} \right\} d\xi \\ sim_{pl,i}(\xi) = \Delta_{3,i} + C\xi^2(1 - 2\xi/3) \end{cases}. \tag{6}$$

Similarly, for a spherical wave ($\overline{\Theta} = 1$), the weighting function is modified accordingly, and the saturated SI can be written as

$$\sigma_{S,sp}^2(L) = 1 + 2\pi\beta_0 \varepsilon^{-1/3} L^3 \left(A^2 \chi_T W_{T,sp} + B^2 \chi_S W_{S,sp} + 2AB\chi_{TS} W_{TS,sp} \right), \tag{7}$$

where the $W_{i,sp}$ is:

$$\begin{cases} W_{i,sp} = \int_0^1 \xi^2 (1-\xi)^2 \left\{ \dfrac{0.4639}{\left[sim_{sp,i}(\xi)\right]^{\frac{7}{6}}} + \dfrac{0.4428\Delta_{1,i}}{\left[sim_{sp,i}(\xi)\right]^{\frac{7}{6}+\frac{0.61}{2}}} - \dfrac{0.4429\Delta_{2,i}}{\left[sim_{sp,i}(\xi)\right]^{\frac{7}{6}+\frac{0.55}{2}}} \right\} d\xi \\ sim_{sp,i}(\xi) = \Delta_{3,i} + C\xi^2(1-\xi)^2/3 \end{cases}. \tag{8}$$

Because the Gaussian-beam formulation shares the same asymptotic structure as the plane-wave and spherical-wave cases, its saturated SI can be represented by a weighted combination of the two limiting solutions [6], i.e.,

$$\sigma_S^2(0,L) = 1 + \left[\sigma_{S,pl}^2(L) - 1\right](1 - \overline{\Theta}) + \left[\sigma_{S,sp}^2(L) - 1\right]\overline{\Theta}. \tag{9}$$

It is readily verified that (9) reduces to the plane-wave result when $\overline{\Theta} = 0$ and to the spherical-wave result when $\overline{\Theta} = 1$. Hence, the saturated-turbulence SI expressions of the three beam types are established and will serve as the upper-bound constraints for constructing the unified scintillation model in the next subsection.

2.2. Unified Scintillation Model Under Arbitrary Oceanic Turbulence

The weak-turbulence SI reported in [16] and the saturated-turbulence boundary solution derived in Section 2.1 represent two asymptotic limits of scintillation behavior. To construct a general model valid for arbitrary oceanic turbulence intensity, it is necessary

to establish a unified SI expression that is equivalent to the weak-turbulence result in the low-fluctuation regime and reduces to the saturated solution in the strong-fluctuation limit. For the intermediate regime, namely moderate-to-strong turbulence, the scintillation behavior can be analyzed within the framework of the extended Rytov approximation. It should be noted that, in the theory of optical scintillation, closed-form analytical results are generally available only in the weak-fluctuation and saturated strong-fluctuation limits. For the intermediate moderate-to-strong fluctuation regime, the extended Rytov method commonly constructs a bridging formulation between these two asymptotic limits by introducing large-scale and small-scale fluctuation components and effective spatial filtering functions [6,18]. In the present oceanic-turbulence case, this procedure is reformulated using the general OTOPS, and the cutoff spatial frequencies are re-determined according to the weak- and saturated-turbulence boundary constraints. Based on this treatment, the main contribution of this work is to derive a closed-form SI expression for Gaussian laser beams under arbitrary oceanic turbulence strength within the general OTOPS framework. This distinguishes the present model from atmospheric unified scintillation models that directly inherit atmospheric cutoff-frequency treatments. This interpolation form is selected because it preserves the large-scale/small-scale decomposition of the extended Rytov framework and satisfies the required weak- and saturated-limit constraints. The fitting parameters are therefore determined by enforcing these asymptotic constraints, rather than by freely fitting arbitrary curves.

To this end, an effective general OTOPS is introduced by incorporating large-scale and small-scale spatial filtering functions into the original spectrum. This treatment removes the contribution of intermediate-scale eddies that become ineffective due to the loss of spatial coherence during propagation. Accordingly, the effective spectrum can be expressed as [6]

$$\Phi_{n,e}(\kappa) = \Phi_n(\kappa)G(\kappa) = \Phi_n(\kappa)[G_X(\kappa) + G_Y(\kappa)] = \Phi_{n,X}(\kappa) + \Phi_{n,Y}(\kappa), \tag{10}$$

where $\Phi_{n,e}(\kappa)$ denotes the effective oceanic turbulence optical power spectrum, $\Phi_n(\kappa)$ is the original general OTOPS, and $G(\kappa)$ is the composite spatial filter. Here, $G_X(\kappa)$ and $G_Y(\kappa)$ represent the large-scale and small-scale spatial filtering functions, respectively; $\Phi_{n,X}(\kappa) = \Phi_n(\kappa)G_X(\kappa)$ and $\Phi_{n,Y}(\kappa) = \Phi_n(\kappa)G_Y(\kappa)$ denote the large-scale and small-scale components of the effective spectrum. Under weak turbulence, the effective OTOPS reduces to the original spectrum because all turbulence scales contribute to refraction and diffraction. Under moderate-to-strong turbulence, however, only the spatial-frequency components contributing to the final irradiance fluctuations are retained. The corresponding large-scale and small-scale filters are defined as

$$\begin{cases} G_X(\kappa) = \exp\left(-\frac{\kappa^2}{\kappa_X^2}\right) \\ G_Y(\kappa) = \frac{\kappa^{11/3}}{\left(\kappa^2+\kappa_Y^2\right)^{11/6}} \end{cases}, \tag{11}$$

where κ_X and κ_Y denote the large-scale and small-scale cutoff spatial frequencies, respectively. The filter $G_X(\kappa)$ retains the low-spatial-frequency components mainly associated with refraction, whereas $G_Y(\kappa)$ retains the high-spatial-frequency components mainly associated with diffraction.

The effective filtering treatment is determined by three characteristic scales, namely, the coherence radius ρ_0, the Fresnel zone $\sqrt{L/k}$, and the scattering disk $L/k\rho_0$, together with their corresponding spatial frequencies.

$$\begin{cases} (l_1, l_2, l_3) \sim (\rho_0, \sqrt{L/k}, L/k\rho_0) \\ (\kappa_1, \kappa_2, \kappa_3) \sim (1/\rho_0, \sqrt{k/L}, k\rho_0/L) \end{cases}. \tag{12}$$

In weak turbulence, eddies smaller than the Fresnel zone mainly contribute to diffraction, whereas larger eddies mainly contribute to refraction. As the turbulence strength increases, the coherence radius becomes smaller than the Fresnel zone, while the scattering disk becomes larger. Therefore, the cutoff spatial frequencies introduced in the large-scale and small-scale filters satisfy the following asymptotic relations [18]:

$$\kappa_X \sim \begin{cases} \kappa_2, & L/k\rho_0^2 \ll 1 \\ \kappa_3, & L/k\rho_0^2 \gg 1 \end{cases}, \tag{13}$$

$$\kappa_Y \sim \begin{cases} \kappa_2, & L/k\rho_0^2 \ll 1 \\ \kappa_1, & L/k\rho_0^2 \gg 1 \end{cases}. \tag{14}$$

For convenience, the dimensionless parameter, $\eta_H = L\kappa^2/k$, is introduced to characterize the relative scale between the Fresnel zone and turbulence eddies. Accordingly, the characteristic spatial frequencies in (12) can be rewritten in dimensionless form as

$$\begin{cases} L\kappa_1^2/k \sim L/k\rho_0^2 \\ L\kappa_2^2/k \sim 1 \\ L\kappa_3^2/k \sim k\rho_0^2/L \end{cases}. \tag{15}$$

The relative positions of the characteristic scales in the weak- and strong-turbulence limits are illustrated in Figure 1. Based on this scale separation, the effective cutoff spatial frequencies κ_X and κ_Y are introduced as follows:

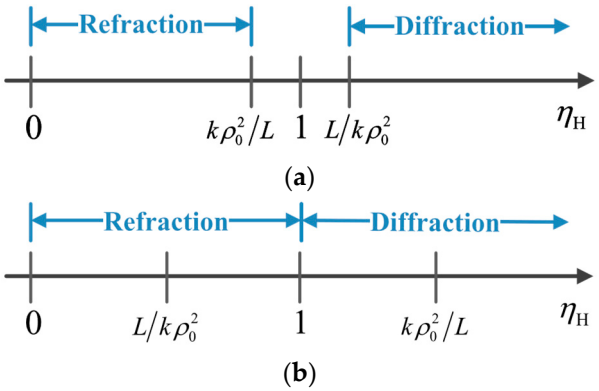


Figure 1. Relative positions of characteristic turbulence scales in the weak- and strong-turbulence limits: (**a**) weak turbulence; (**b**) strong turbulence.

Based on the scale separation shown in Figure 1a,b, two effective scales are introduced to determine the cutoff spatial frequencies κ_X and κ_Y namely, the effective scattering disk $L/(kl_X)$ and the effective coherence length l_Y. Accordingly, the corresponding cutoff spatial frequencies are written as

$$\left(\frac{L}{kl_X}\right)^2 = \frac{1}{\kappa_X^2} = \frac{c_1}{\kappa_2^2} + \frac{c_2}{\kappa_3^2} = \frac{c_1 L}{k} + c_2\left(\frac{L}{k\rho_0}\right)^2, \tag{16}$$

$$\frac{1}{l_Y^2} = \kappa_Y^2 = c_3\kappa_2^2 + c_4\kappa_1^2 = \frac{c_3}{L/k} + \frac{c_4}{\rho_0^2}, \tag{17}$$

where c_1, c_2, c_3, and c_4 are undetermined constants to be specified later for different beam types. Here, c_1 and c_2 are associated with the large-scale fluctuation parameter η_X, while c_3 and c_4 are associated with the small-scale fluctuation parameter η_Y.

Following the definition of the dimensionless parameter $\eta_H = L_{\kappa^2}/k$, the corresponding large-scale and small-scale dimensionless quantities are introduced as

$$\eta_X = \frac{L\kappa_X^2}{k} = \frac{1}{c_1 + c_2 L/k\rho_0^2} \sim \begin{cases} 1/c_1, & L/k\rho_0^2 \ll 1 \\ k\rho_0^2/c_2 L, & L/k\rho_0^2 \gg 1 \end{cases}, \tag{18}$$

$$\eta_Y = \frac{L\kappa_Y^2}{k} = c_3 + c_4 \frac{L}{k\rho_0^2} \sim \begin{cases} c_3, & L/k\rho_0^2 \ll 1 \\ c_4 L/k\rho_0^2, & L/k\rho_0^2 \gg 1 \end{cases}. \tag{19}$$

It is seen that η_X and η_Y depend on the four unknown constants c_1–c_4. These constants will be determined later by asymptotic matching with the weak- and saturated-turbulence limits.

For a Gaussian beam propagating along a horizontal path, the large-scale log-irradiance fluctuation is defined as [6]

$$\sigma^2_{\ln X,gs} = 8\pi^2 k^2 L \int_0^1 \int_0^\infty \kappa \Phi_n(\kappa) G_X(\kappa) \exp\left(-\frac{\Lambda L \kappa^2 \xi^2}{k}\right) \left[1 - \cos\left(\frac{L\kappa^2}{k}\xi\left(1 - \overline{\Theta}\xi\right)\right)\right] d\kappa d\xi \tag{20}$$

Since the large-scale filter $G_X(\kappa)$ only retains the low-spatial-frequency components, the geometric optics approximation can be applied. Under this condition, the approximations

$$1 - \cos(\Psi); \Psi^2/2, \ \exp\left(-\frac{\Lambda L \kappa^2 \xi^2}{k}\right) \cong 1, \tag{21}$$

hold, and Formulas (11), (20) and (21) can be simplified accordingly.

By substituting the general OTOPS reported in [10] and the large-scale filter given in (11) into (20), one obtains

$$\sigma^2_{\ln X,gs} = A^2 \sigma^2_{\ln X,gs,T} + B^2 \sigma^2_{\ln X,gs,S} + 2AB\sigma^2_{\ln X,gs,TS}, \tag{22}$$

where $\sigma^2_{\ln X,gs,i}$ is

$$\begin{aligned} \sigma^2_{\ln X,gs,i} &= \pi\beta_0 \varepsilon^{-1/3} \chi_i L^3 \textstyle\int_0^1 \xi^2 \left(1 - \overline{\Theta}\xi\right)^2 d\xi \\ &\times \textstyle\int_0^\infty \kappa^{4/3} \left[1 + \Delta_{1,i}\kappa^{0.61} - \Delta_{2,i}\kappa^{0.55}\right] \exp\left(-\Delta_{3,i}\kappa^2\right) \exp\left(-\frac{\kappa^2}{\kappa_X^2}\right) d\kappa. \end{aligned} \tag{23}$$

By performing the integrations and rearranging the result, the large-scale log-irradiance fluctuation of the Gaussian beam can be written in compact form as

$$\sigma^2_{\ln X,gs} = 0.49\sigma_1^2 \left(\frac{1}{3} + \frac{\overline{\Theta}^2}{5} - \frac{\overline{\Theta}}{2}\right) \left[A^2 \chi_T \widetilde{Y}_T + B^2 \chi_S \widetilde{Y}_S + 2AB\chi_{TS}\widetilde{Y}_{TS}\right], \tag{24}$$

where $\widetilde{Y}_i$ is

$$\widetilde{Y}_i = \left(\frac{\eta_{X,gs} Q_{\eta,i}}{\eta_{X,gs} + Q_{\eta,i}}\right)^{\frac{7}{6}} \left[1 + \frac{4.2697}{c_i^{0.2728}} \left(\frac{\eta_{X,gs}}{\eta_{X,gs} + Q_{\eta,i}}\right)^{\frac{0.61}{2}} - \frac{4.1949}{c_i^{0.224}} \left(\frac{\eta_{X,gs}}{\eta_{X,gs} + Q_{\eta,i}}\right)^{\frac{0.55}{2}}\right], \tag{25}$$

where $i \in \{T, S, TS\}$, and $Q_{\eta,i} = L\kappa_{\eta,i}^2/k$ denotes the dimensionless inner-scale parameter for the $i-$th OTOPS component.

Similarly, the small-scale log-irradiance fluctuation of the Gaussian beam is defined as [6]

$$\sigma^2_{\ln Y,gs} = 8\pi^2 k^2 L \int_0^1 \int_0^\infty \kappa \Phi_n(\kappa) G_Y(\kappa) \exp\left(-\frac{\Lambda L \kappa^2 \xi^2}{k}\right)\left[1 - \cos\left(\frac{L\kappa^2}{k}\xi\left(1 - \overline{\Theta}\xi\right)\right)\right] d\kappa d\xi \tag{26}$$

For Gaussian beams, the small-scale filter should be modified to include the propagation-dependent factor (11), i.e.,

$$G_Y(\kappa, \xi) = \frac{\kappa^{11/3}}{\left(\kappa^2 + \kappa_Y^2\right)^{11/6}} \exp\left(\frac{\Lambda L \kappa^2 \xi^2}{k}\right),\ \kappa_Y \gg 1. \tag{27}$$

This modification reflects the gradual suppression of finite-beam characteristics over sufficiently long propagation distances, under which the Gaussian beam tends to behave similarly to a spherical wave. Substituting the modified filter and the general OTOPS into the above expression gives

$$\begin{cases} \sigma^2_{\ln Y,gs} = A^2 \sigma^2_{\ln Y,gs,T} + B^2 \sigma^2_{\ln Y,gs,S} + 2AB\sigma^2_{\ln Y,gs,TS} \\ \sigma^2_{\ln Y,gs,i} = 2\pi\beta_0 \varepsilon^{-1/3} \chi_i k^2 L \int_0^\infty \dfrac{\kappa}{\left(\kappa^2 + \kappa_Y^2\right)^{11/6}} \left[1 + \Delta_{1,i}\kappa^{0.61} - \Delta_{2,i}\kappa^{0.55}\right] \exp\left(-\dfrac{\kappa^2}{\kappa_{\eta,i}{}^2}\right) d\kappa \end{cases} \tag{28}$$

After evaluating the integral and simplifying the result, the small-scale log-irradiance fluctuation can be expressed in compact form as

$$\sigma^2_{\ln Y,gs} = 1.06\sigma_1^2 \eta_{Y,gs}^{-5/6}\left[A^2\chi_T H_T + B^2\chi_S H_S + 2AB\chi_{TS} H_{TS}\right], \tag{29}$$

where H_i is

$$H_i = \begin{Bmatrix} \Gamma(1) U\left(1; \frac{1}{6}; \frac{\Delta_{3,i} k\eta_{Y,gs}}{L}\right) \\ +\Delta_{1,i}\left(\frac{k\eta_{Y,gs}}{L}\right)^{\frac{0.61}{2}} \Gamma\left(1 + \frac{0.61}{2}\right) U\left(1 + \frac{0.61}{2}; \frac{1}{6} + \frac{0.61}{2}; \frac{\Delta_{3,i} k\eta_{Y,gs}}{L}\right) \\ -\Delta_{2,i}\left(\frac{k\eta_{Y,gs}}{L}\right)^{\frac{0.55}{2}} \Gamma\left(1 + \frac{0.55}{2}\right) U\left(1 + \frac{0.55}{2}; \frac{1}{6} + \frac{0.55}{2}; \frac{\Delta_{3,i} k\eta_{Y,gs}}{L}\right) \end{Bmatrix}. \tag{30}$$

Accordingly, using Formulas (24) and (29), the scintillation index of the Gaussian beam under arbitrary oceanic turbulence intensity is obtained as

$$\sigma^2_{I,gs} = \exp\left[\sigma^2_{\ln X,gs} + \sigma^2_{\ln Y,gs}\right] - 1. \tag{31}$$

To avoid an unnecessarily lengthy derivation, the corresponding expressions for the plane wave and spherical wave are not repeated here in full detail. They can be obtained from the same extended Rytov procedure by taking the corresponding limiting beam parameters, which leads to the total SI expressions

$$\begin{cases} \sigma^2_{I,pl} = \exp\left[\sigma^2_{\ln X,pl} + \sigma^2_{\ln Y,pl}\right] - 1, \text{ for a plane wave} \\ \sigma^2_{I,sp} = \exp\left[\sigma^2_{\ln X,sp} + \sigma^2_{\ln Y,sp}\right] - 1, \text{ for a spherical wave} \end{cases}. \tag{32}$$

The remaining task is to determine the undetermined constants c_1–c_4 embedded in the dimensionless parameters η_X and η_Y. This is achieved by asymptotic matching in the weak- and strong-fluctuation limits. The constants c_1–c_4 are determined by a constraint-based asymptotic matching procedure rather than by unconstrained empirical fitting. Specifically, the weak-turbulence SI obtained from the Rytov approximation and the saturated-turbulence SI obtained from asymptotic theory are used as the two limiting constraints.

The parameters (c_1, c_2) and (c_3, c_4) are introduced into the large-scale and small-scale cutoff quantities, respectively, and are then fixed by requiring the unified expression to recover the weak-fluctuation limit ($L/k\rho_0^2 \ll 1$) and the saturated strong-fluctuation limit ($L/k\rho_0^2 \gg 1$). Thus, the fitting criterion is the exact recovery of the two asymptotic limits. For the Gaussian beam, the corresponding constraints can be summarized as follows

$$\begin{cases} \sigma^2_{\ln X,gs} = 0.49\sigma_G^2 \\ \sigma^2_{\ln Y,gs} = 0.51\sigma_G^2 \end{cases}, \; L/k\rho_0^2 \ll 1, \tag{33}$$

$$\begin{cases} \sigma_S^2(0,L) \cong 2\sigma^2_{\ln X,gs} + 1 \\ \sigma^2_{\ln Y,gs} = \ln 2 \end{cases}, \; L/k\rho_0^2 \gg 1\,. \tag{34}$$

By solving the resulting asymptotic matching conditions, the parameter set is obtained as

$$\text{Gaussian beam} \begin{cases} c_1 = 0.4793, \; c_3 = 2.9171 \\ c_2 = 0.2551, \; c_4 = 1.1468 \end{cases}. \tag{35}$$

Since these constants are fixed by asymptotic constraints rather than by regression against experimental or simulation data, no separate least-squares error metric is involved in their determination.

Substituting this parameter set into the corresponding dimensionless quantities yields

$$\text{Gaussian beam} \begin{cases} \eta_{X,gs} = \frac{1}{0.4793+0.2551L/k\rho_0^2} \sim \begin{cases} 2.0864, & L/k\rho_0^2 \ll 1 \\ \frac{k\rho_0^2}{0.2551L}, & L/k\rho_0^2 \gg 1 \end{cases} \\ \eta_{Y,gs} = 2.9171 + 1.1468L/k\rho_0^2 \sim \begin{cases} 2.9171, & L/k\rho_0^2 \ll 1 \\ \frac{1.1468L}{k\rho_0^2}, & L/k\rho_0^2 \gg 1 \end{cases} \end{cases}. \tag{36}$$

Similarly, the parameter sets for the plane wave and spherical wave are given by

$$\text{plane wave} \begin{cases} c_1 = 0.4644, \; c_3 = 2.8410 \\ c_2 = 0.3193, \; c_4 = 1.1468 \end{cases}, \tag{37}$$

$$\text{spherical wave} \begin{cases} c_1 = 0.1429, \; c_3 = 9.3420 \\ c_2 = 0.0178, \; c_4 = 1.1468 \end{cases}, \tag{38}$$

and the corresponding dimensionless quantities become

$$\text{plane wave} \begin{cases} \eta_{X,pl} = \frac{1}{0.4644+0.3193L/k\rho_0^2} \sim \begin{cases} 2.1533, & L/k\rho_0^2 \ll 1 \\ \frac{k\rho_0^2}{0.3193L}, & L/k\rho_0^2 \gg 1 \end{cases} \\ \eta_{Y,pl} = 2.8410 + 1.1468L/k\rho_0^2 \sim \begin{cases} 2.8410, & L/k\rho_0^2 \ll 1 \\ \frac{1.1468L}{k\rho_0^2}, & L/k\rho_0^2 \gg 1 \end{cases} \end{cases}, \tag{39}$$

$$\text{spherical wave} \begin{cases} \eta_{X,sp} = \frac{1}{0.1429+0.0178L/k\rho_0^2} \sim \begin{cases} 6.9979, & L/k\rho_0^2 \ll 1 \\ \frac{k\rho_0^2}{0.0178L}, & L/k\rho_0^2 \gg 1 \end{cases} \\ \eta_{Y,sp} = 9.3420 + 1.1468L/k\rho_0^2 \sim \begin{cases} 9.3420, & L/k\rho_0^2 \ll 1 \\ \frac{1.1468L}{k\rho_0^2}, & L/k\rho_0^2 \gg 1 \end{cases} \end{cases}. \tag{40}$$

With these fitted parameters, the unified scintillation model valid for arbitrary oceanic turbulence intensity is fully determined. For convenience, the final SI expressions of the Gaussian beam, plane wave, and spherical wave are summarized in Table 1. The proposed model provides a smooth transition from weak turbulence to saturated strong turbulence and will be validated numerically in the next section.

Table 1. Final unified SI expressions and fitted dimensionless parameters for three beam types under arbitrary oceanic turbulence.

Beam Type	Final SI Expression	η_X	η_Y
Gaussian beam	$\sigma_{I,gs}^2 = \exp\left[\sigma_{\ln X,gs}^2 + \sigma_{\ln Y,gs}^2\right] - 1$	$\eta_{X,gs} = \frac{1}{0.4793+0.2551L/k\rho_0^2}$	$\eta_{Y,gs} = 2.9171 + 1.1468L/k\rho_0^2$
Plane wave	$\sigma_{I,pl}^2 = \exp\left[\sigma_{\ln X,pl}^2 + \sigma_{\ln Y,pl}^2\right] - 1$	$\eta_{X,pl} = \frac{1}{0.4644+0.3193L/k\rho_0^2}$	$\eta_{Y,pl} = 2.8410 + 1.1468L/k\rho_0^2$
Spherical wave	$\sigma_{I,sp}^2 = \exp\left[\sigma_{\ln X,sp}^2 + \sigma_{\ln Y,sp}^2\right] - 1$	$\eta_{X,sp} = \frac{1}{0.1429+0.0178L/k\rho_0^2}$	$\eta_{Y,sp} = 9.3420 + 1.1468L/k\rho_0^2$

2.3. Gamma–Gamma Probability Density Function and Bit Error Rate

To evaluate the performance of UWOC systems, the probability density function (PDF) of the received irradiance must be specified in addition to the scintillation index. The Gamma–Gamma distribution has been widely used and validated as an effective statistical model for irradiance fluctuations in moderate-to-strong atmospheric turbulence. Since both atmospheric and oceanic turbulence affect laser-beam propagation through random refractive-index fluctuations, the irradiance fluctuation mechanisms in these two media share certain physical similarities. This provides the basic motivation for adopting a Gamma–Gamma-type model in oceanic turbulence.

This choice is further supported by previous UWOC studies, where the Gamma–Gamma distribution has been used to model moderate-to-strong underwater optical turbulence channels [19–21]. Within the extended Rytov framework, the normalized irradiance can be interpreted as the product of two independent modulation processes associated with large-scale and small-scale eddies. The corresponding log-irradiance variances have similar physical interpretations in atmospheric and oceanic media, which provides the physical basis for approximating oceanic irradiance fluctuations by the Gamma–Gamma distribution.

Accordingly, the large-scale and small-scale irradiance components are assumed to follow Gamma distributions. By combining these two components, the Gamma–Gamma PDF of the received irradiance is obtained as [19]

$$\begin{aligned} f_I(I) &= \int_0^\infty f_Y(I|X) f_X(X) dX \\ &= \frac{2(\alpha_g\beta_g)^{\frac{\alpha_g+\beta_g}{2}}}{\Gamma(\alpha_g)\Gamma(\beta_g)} I^{\frac{\alpha_g+\beta_g}{2}-1} K_{\alpha_g-\beta_g}\left(2\sqrt{\alpha_g\beta_g I},\right),\ I>0 \end{aligned} \tag{41}$$

where $K_l(x)$ denotes the modified Bessel function of the second kind of order l. The parameters α_g and β_g in the Gamma–Gamma PDF are directly related to the large-scale and small-scale log-irradiance fluctuations, a $\sigma_{\ln X}^2$ and $\sigma_{\ln Y}^2$, respectively, and are given by

$$\alpha_g = \frac{1}{\exp(\sigma_{\ln X}^2) - 1}, \tag{42}$$

$$\beta_g = \frac{1}{\exp(\sigma_{\ln Y}^2) - 1}. \tag{43}$$

For an UWOC system employing OOK modulation, the average bit error rate (BER) is obtained by averaging the conditional BER over the irradiance PDF. Accordingly, the average BER can be written as

$$\langle BER \rangle = \frac{1}{2}\int_0^\infty f_I(I) erfc\left(\frac{\langle SNR \rangle I}{2\sqrt{2}}\right) dI, \tag{44}$$

which provides the basis for performance evaluation under arbitrary oceanic turbulence intensity. The corresponding numerical results are presented in Section 3.

It should be emphasized that this assumption should be interpreted with caution. Although the unified SI model developed in Section 2.2 provides an analytical description over a wide range of oceanic turbulence strengths, the exact irradiance PDF in strong or saturated oceanic turbulence has not yet been comprehensively verified by real-ocean measurements. Oceanic turbulence may involve temperature-salinity coupling, absorption, scattering, and water-parameter dependence, which may lead to deviations from the ideal Gamma–Gamma model. Therefore, the Gamma–Gamma distribution is adopted here as a tractable approximate statistical model for BER evaluation, rather than as a rigorously proven universal PDF for all oceanic turbulence conditions.

3. Simulation Results and Discussions

Before presenting the numerical results, the main simulation parameters used in the numerical calculations are summarized in Table 2. Unless otherwise specified, these parameters are used for all figures in this section. When a parameter is used as the independent variable in a specific figure, its value is varied according to the corresponding axis or figure caption, while the other parameters remain the same as those listed in Table 2. The use of this common parameter set facilitates the reproducibility of the numerical results presented in the following simulation Figures 2–8.

Table 2. Simulation parameters used in the numerical calculations.

Parameter	Value/Unit
Phase front radius of curvature F_0	∞
Initial beam radius W_0	3 mm
Optical wavelength λ	532 nm
Propagation distance L	20 m
Kinetic energy dissipation rate ε	10^{-2} m^{2}s^{-3}
Temperature variance dissipation rate χ_T	10^{-4} K^{2}s^{-1}
Kolmogorov microscale η	10^{-3} m
Average temperature $\langle T \rangle$	20 °C
Average salinity $\langle S \rangle$	34.9 ppt
Temperature-salinity gradient ratio H	-10 °C · ppt^{-1}

3.1. Validation of the Unified SI Model

To validate the proposed unified scintillation model, the SI results of the Gaussian beam, plane wave, and spherical wave are first compared with the corresponding weak-turbulence solutions reported in [13] and the saturated-turbulence boundary solutions derived in Section 2.1. Since the purpose of the unified model is to provide a smooth transition from weak turbulence to saturated strong turbulence, the general SI expression is expected to recover the weak-turbulence result in the low-fluctuation regime and the saturated solution in the strong-fluctuation regime.

Figure 2a–c shows that, for all three beam types, the unified SI curves agree well with the corresponding boundary solutions in the two limiting regions, while preserving the characteristic "bump" behavior in the moderate-to-strong turbulence regime. This

confirms that the asymptotic matching procedure adopted in Section 2 yields a reasonable transition between the weak- and strong-fluctuation limits. The small deviations observed near the transition regions are acceptable and consistent with the interpolation nature of the unified formulation.

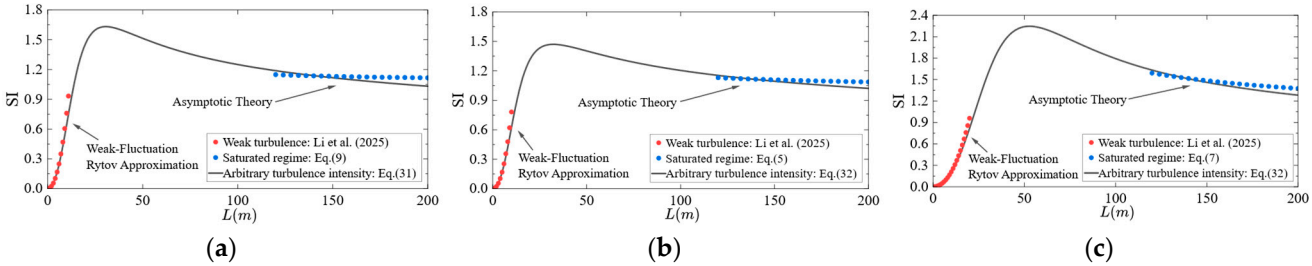


Figure 2. Unified scintillation index (SI) of (**a**) the Gaussian beam, (**b**) the plane wave, and (**c**) the spherical wave versus propagation distance, together with the corresponding weak-turbulence solution reported by Li et al. [16] and the saturated-turbulence boundary solutions.

For all three beam types, the SI increases rapidly with propagation distance in the weak-turbulence region, reaches a peak in the moderate-to-strong turbulence regime, and then gradually decreases toward a saturated value. At relatively short distances, random focusing induced by turbulence accumulates and enhances the irradiance fluctuation. As the distance increases further, multiple scattering and the loss of spatial coherence reduce the contribution of effective eddies, so that the scintillation weakens and finally approaches saturation. This behavior is physically consistent with the general propagation law in random media.

To further compare the three beam types, their unified SI curves can be plotted together with the large-scale and small-scale log-irradiance fluctuations of the Gaussian beam.

Figure 3 indicates that the relative scintillation strengths of different beam types depend on the propagation distance. In particular, the spherical wave exhibits a higher SI peak and reaches that peak at a longer distance, whereas the plane wave and Gaussian beam tend to approach the saturated regime earlier. These observations further support the physical consistency of the proposed unified model.

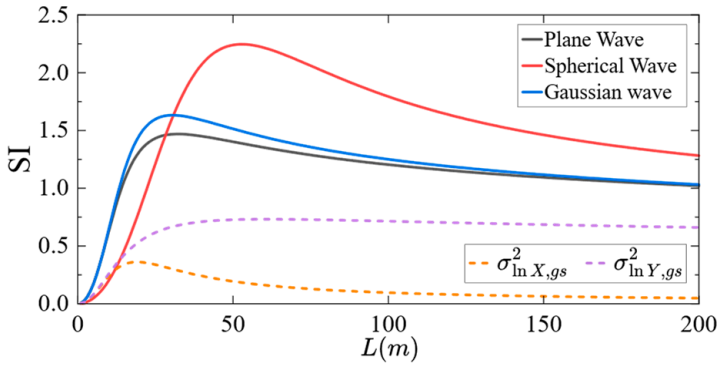


Figure 3. Comparison of the unified SI for three beam types and the large-scale and small-scale log-irradiance fluctuations of the Gaussian beam.

3.2. Comparison with Existing Models

To examine the difference between the proposed oceanic extended-Rytov formulation and an existing analytical model, the present results are compared with the model reported in [18]. In that model, the atmospheric moderate-to-strong turbulence SI formulation was combined directly with the weak-oceanic-turbulence Rytov variance of a Gaussian beam, without re-establishing the oceanic cutoff spatial frequencies.

As shown in Figure 4, the discrepancy first appears at the level of the large-scale and small-scale log-irradiance fluctuations. The present model predicts a more pronounced large-scale peak and a stronger small-scale contribution over a broad propagation range, whereas the model in [18] gives a smoother transition in the peak region. This difference mainly arises from the treatment of the cutoff spatial frequencies, indicating that the oceanic cutoff spatial frequencies should not be directly inherited from the atmospheric formulation but need to be re-determined from the weak- and saturated-turbulence boundary conditions.

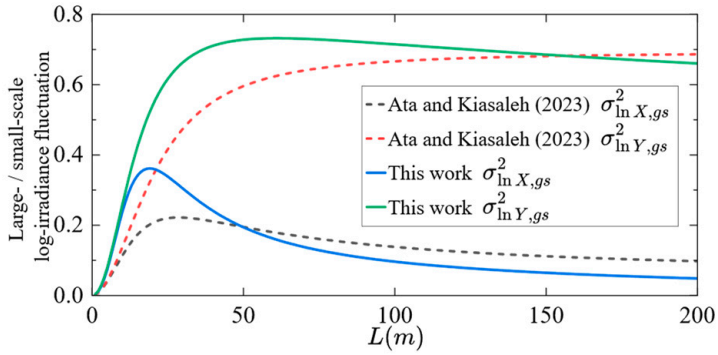


Figure 4. Comparison of the large-scale and small-scale log-irradiance fluctuations of the Gaussian beam predicted by the proposed model and by the model in [20].

The impact of this different cutoff-frequency treatment is further reflected in the total SI curves shown in Figure 5. For all three beam types, the proposed model produces a more evident "bump" feature near the peak region and predicts higher peak values at shorter propagation distances. In contrast, the model in [18] gives a smoother peak-region variation and a slower decay after the peak. These differences do not, by themselves, constitute direct experimental proof of accuracy in the intermediate regime. Instead, they indicate that re-establishing the effective cutoff spatial frequencies under the oceanic OTOPS framework can lead to a different physical prediction from that obtained by directly inheriting the atmospheric formulation. The present comparison is therefore used to illustrate the influence of ocean-specific scale separation on scintillation modeling.

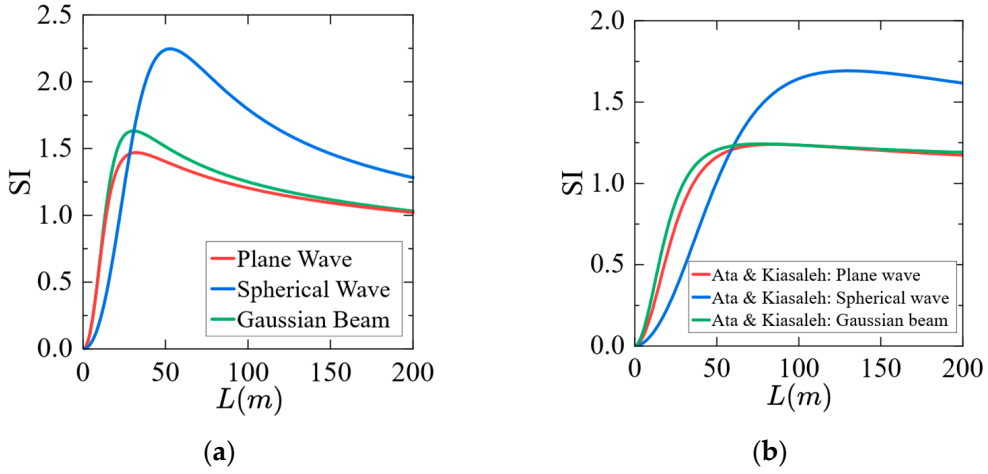


Figure 5. Comparison of the unified scintillation index versus propagation distance for the plane wave, spherical wave, and Gaussian beam predicted by (**a**) the proposed model and (**b**) the model in [20].

3.3. BER Performance Analysis

To further evaluate the communication impact of the proposed scintillation model, the BER performance of UWOC systems is analyzed by combining the unified SI with the Gamma–Gamma PDF introduced in Section 2.3.

As shown in Figure 6, $\langle BER \rangle$—the average bit error rate, which quantifies the reliability of communication systems—decreases monotonically with the average output signal-to-noise ratio, denoted as $\langle SNR \rangle$, for all three beam types, as expected. For a given beam type, a longer propagation distance generally requires a higher output SNR to achieve the same BER performance. This trend aligns with the corresponding increase in the scintillation index (SI) with propagation distance before the onset of scintillation saturation. Once the propagation distance becomes sufficiently large and the channel enters the saturated regime, the BER curves for different distances gradually converge, indicating that the dependence of BER on propagation distance weakens after scintillation saturation.

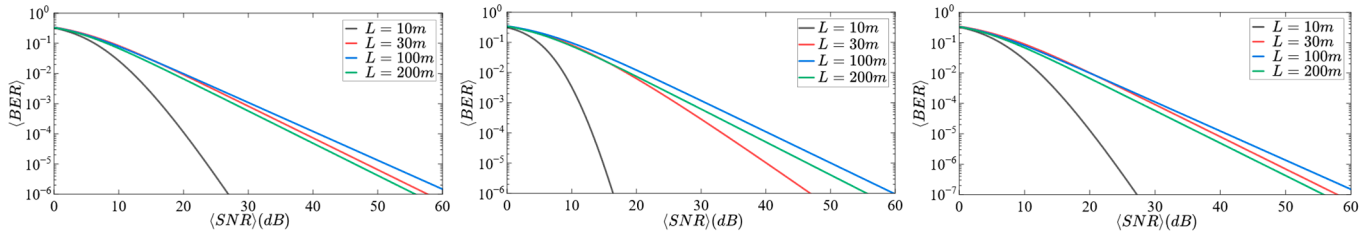


Figure 6. $\langle BER \rangle$ versus $\langle SNR \rangle$ for different propagation distances L for (**a**) the plane wave, (**b**) the spherical wave, and (**c**) the Gaussian beam.

The BER curves also reveal noticeable differences among beam types. Under the same propagation conditions, the beam with a lower scintillation level generally exhibits better communication performance. In particular, when the spherical wave has a lower SI than the plane wave at a given distance, it correspondingly requires a lower output SNR to achieve the same BER target. This observation is fully consistent with the SI comparisons presented above and further confirms the physical reliability of the proposed unified model.

Figure 7 provides a more direct comparison of beam-type dependence at a fixed propagation distance. It can be seen that the spherical wave may outperform the plane wave under certain propagation conditions because of its relatively lower scintillation level in that regime. In addition, a wide Gaussian beam exhibits BER performance very close to that of a plane wave, which agrees well with the corresponding SI behavior and reflects the fact that a sufficiently wide Gaussian beam approaches the plane-wave limit.

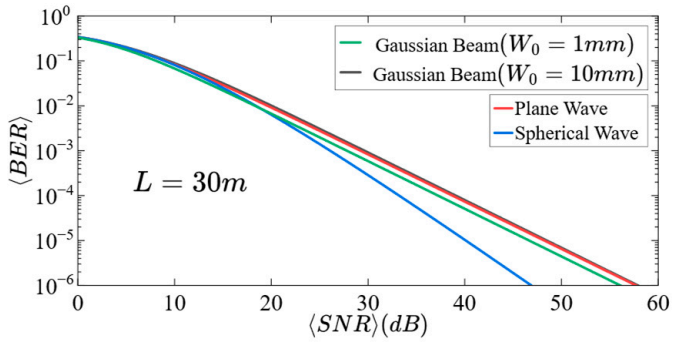


Figure 7. $\langle BER \rangle$ versus $\langle SNR \rangle$ at a propagation distance of $L = 30$ m.

If the influence of the turbulence inner scale is to be emphasized, Figure 8 may be included.

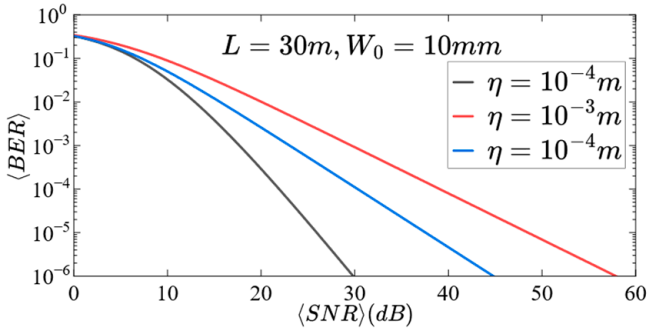


Figure 8. $\langle BER \rangle$ versus $\langle SNR \rangle$ for different turbulence inner scales.

When the inner scale is varied, the required output SNR for achieving a given BER changes nonlinearly, which is consistent with the non-monotonic dependence already observed in the SI results. This again indicates that the BER behavior is governed directly by the underlying scintillation characteristics and therefore provides an additional validation of the proposed unified model.

Overall, the BER analysis confirms that the proposed unified SI model, together with the Gamma–Gamma PDF, provides an effective framework for evaluating UWOC system performance under arbitrary oceanic turbulence intensity. Compared with existing approaches, the present model captures the ocean-specific scintillation behavior more accurately and therefore yields more reliable performance predictions.

4. Conclusions

A unified closed-form model of irradiance scintillation under arbitrary oceanic turbulence intensity was developed for the Gaussian beam, plane wave, and spherical wave. By combining the weak-turbulence boundary with the saturated-turbulence boundary through asymptotic matching, the proposed model provides a smooth transition from weak turbulence to saturated strong turbulence. Numerical results show that the unified model agrees well with the corresponding boundary solutions and reproduces the characteristic "bump" behavior expected in oceanic scintillation. Compared with the existing analytical model considered in this work, the proposed formulation predicts higher SI peaks at shorter propagation distances, which highlights the influence of re-determining the cutoff spatial frequencies under the oceanic OTOPS framework. Moreover, by combining the unified scintillation model with the Gamma–Gamma PDF, the BER performance of UWOC systems was evaluated under arbitrary turbulence conditions. These results indicate that the proposed framework provides a physically consistent analytical tool for UWOC channel modeling and performance analysis in oceanic turbulence. Further validation using real-ocean measurements, controlled laboratory simulations, or wave-optics numerical simulations will be pursued in future work.

Author Contributions: Conceptualization, B.F. and W.Z.; methodology, B.F. and W.Z.; software, B.F.; validation, B.F., W.Z. and T.H.; formal analysis, B.F.; investigation, W.Z.; writing—original draft preparation, B.F. and W.Z.; writing—review and editing, X.Y., G.L. and Y.L.; visualization, T.H.; supervision, X.Y. All authors have read and agreed to the published version of the manuscript.

Funding: This research was funded by the National Natural Science Foundation of China (62571390).

Data Availability Statement: The original contributions presented in this study are included in the article. Further inquiries can be directed to the corresponding author.

Conflicts of Interest: The authors declare no conflicts of interest.

References

1. Xu, J.; Zhang, Y. Underwater wireless optical communications: From the lab tank to the real sea. *J. Light. Technol.* **2025**, *43*, 1644–1651. [CrossRef]
2. Ata, Y.; Baykal, Y.; Gökçe, M.C. Analysis of optical wireless MIMO communication in underwater medium. *IEEE Internet Things J.* **2024**, *11*, 20660–20672. [CrossRef]
3. Ji, X.; Yin, H.; Xing, F.; Jing, L.; Shen, Z.; Wang, J.; Liang, Y. A generalized and comprehensive slant channel modeling method for underwater wireless optical communication and its system performance analysis. *Opt. Commun.* **2024**, *557*, 130270. [CrossRef]
4. Nootz, G.; Jarosz, E.; Dalgleish, F.R.; Hou, W. Quantification of optical turbulence in the ocean and its effects on beam propagation. *Appl. Opt.* **2016**, *55*, 8813–8820. [CrossRef] [PubMed]
5. Korotkova, O.; Farwell, N.; Shchepakina, E. Light scintillation in oceanic turbulence. *Waves Random Complex Media* **2012**, *22*, 260–266. [CrossRef]
6. Andrews, L.C.; Phillips, R.L. *Laser Beam Propagation Through Random Media*, 2nd ed.; SPIE Press: Bellingham, WA, USA, 2005.
7. Gabriel, C.; Khalighi, M.; Bourennane, S.; Léon, P.; Rigaud, V. Monte-Carlo-based channel characterization for underwater optical communication systems. *J. Opt. Commun. Netw.* **2013**, *5*, 1–12. [CrossRef]
8. Palitharathna, K.W.S.; Godaliyadda, R.I.; Herath, V.R.; Suraweera, H.A. Relay-assisted optical wireless communications in turbid water. In *Proceedings of the 13th International Conference on Underwater Networks & Systems (WUWNet '18), Shenzhen, China, 3–5 December 2018*; Association for Computing Machinery: New York, NY, USA, 2018; pp. 1–5.
9. Nikishov, V.V.; Nikishov, V.I. Spectrum of turbulent fluctuations of the sea-water refraction index. *Int. J. Fluid Mech. Res.* **2000**, *27*, 82–98. [CrossRef]
10. Elamassie, M.; Uysal, M.; Baykal, Y.; Abdallah, M.; Qaraqe, K. Effect of eddy diffusivity ratio on underwater optical scintillation index. *J. Opt. Soc. Am. A* **2017**, *34*, 1969–1973. [CrossRef] [PubMed]
11. Yao, J.; Zhang, Y.; Wang, R.; Wang, Y.; Wang, X. Practical approximation of the oceanic refractive index spectrum. *Opt. Express* **2017**, *25*, 23283–23292. [CrossRef] [PubMed]
12. Yao, J.R.; Zhang, H.J.; Wang, R.N.; Cai, J.D.; Zhang, Y.; Korotkova, O. Wide-range Prandtl/Schmidt number power spectrum of optical turbulence and its application to oceanic light propagation. *Opt. Express* **2019**, *27*, 27807–27819. [CrossRef] [PubMed]
13. Ata, Y.; Baykal, Y. Scintillations of optical plane and spherical waves in underwater turbulence. *J. Opt. Soc. Am. A* **2014**, *31*, 1552–1556. [CrossRef] [PubMed]
14. Wang, Z.; Zhang, P.; Qiao, C.; Lu, L.; Fan, C.; Ji, X. Scintillation index of Gaussian waves in weak turbulent ocean. *Opt. Commun.* **2016**, *380*, 79–86. [CrossRef]
15. Gökçe, M.C.; Baykal, Y. Aperture averaging and BER for Gaussian beam in underwater oceanic turbulence. *Opt. Commun.* **2018**, *410*, 830–835. [CrossRef]
16. Li, Y.; Yi, X.; Tao, X.; Ata, Y.; Cheng, M.; Zhang, L. General scintillation for Gaussian beam propagating through oceanic turbulence and UWOC system performance evaluation. *Opt. Laser Technol.* **2025**, *180*, 111441. [CrossRef]
17. Yao, J.R.; Elamassie, M.; Korotkova, O. Spatial power spectrum of natural water turbulence with any average temperature, salinity concentration, and light wavelength. *J. Opt. Soc. Am. A* **2020**, *37*, 1614–1621. [CrossRef] [PubMed]
18. Andrews, L.C.; Phillips, R.L.; Hopen, C.Y.; Al-Habash, M.A. Theory of optical scintillation. *J. Opt. Soc. Am. A* **1999**, *16*, 1417–1429. [CrossRef]
19. Fu, Y.; Du, Y. Performance of heterodyne differential phase-shift-keying underwater wireless optical communication systems in gamma-gamma-distributed turbulence. *Appl. Opt.* **2018**, *57*, 2057–2063. [CrossRef] [PubMed]
20. Ata, Y.; Kiasaleh, K. Analysis of optical wireless communication links in turbulent underwater channels with wide range of water parameters. *IEEE Trans. Veh. Technol.* **2023**, *72*, 6363–6374. [CrossRef]
21. He, F.; Du, Y.; Zhang, J.; Fang, W.; Li, B.; Zhu, Y. Bit error rate of pulse position modulation wireless optical communication in gamma-gamma oceanic anisotropic turbulence. *Acta Phys. Sin.* **2019**, *68*, 164206. [CrossRef]

Disclaimer/Publisher's Note: The statements, opinions and data contained in all publications are solely those of the individual author(s) and contributor(s) and not of MDPI and/or the editor(s). MDPI and/or the editor(s) disclaim responsibility for any injury to people or property resulting from any ideas, methods, instructions or products referred to in the content.